Physics of Fluids

RESEARCH ARTICLE | AUGUST 08 2025

Aerodynamic shape effects on fluid–structure coupling vibration of train tail inside a small cross section tunnel

Ting Qin (秦汀) ; Yuan Yao (姚远) ; Yadong Song (宋亚东)

Physics of Fluids 37, 085151 (2025)
https://doi.org/10.1063/5.0281264

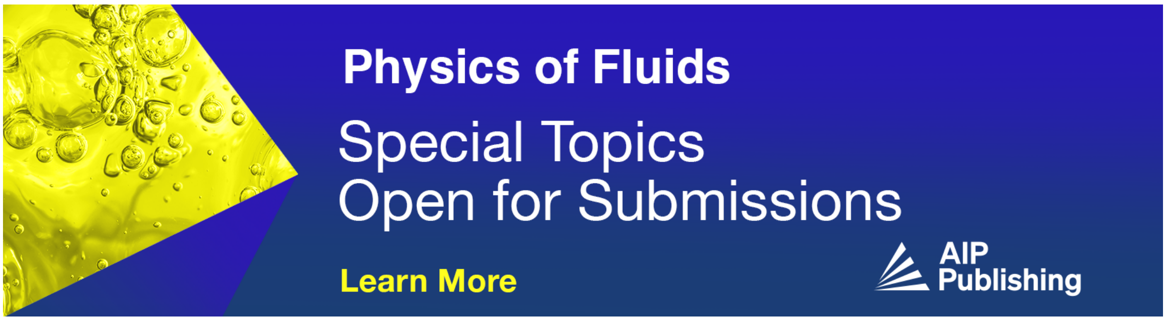

Physics of Fluids ARTICLE pubs.aip.org/aip/pof

Aerodynamic shape effects on fluid–structure coupling vibration of train tail inside a small cross section tunnel

Cite as: Phys. Fluids **37**, 085151 (2025); doi: 10.1063/5.0281264
Submitted: 17 May 2025 · Accepted: 6 July 2025 ·
Published Online: 8 August 2025

Ting Qin (秦汀),[1] Yuan Yao (姚远),[1,a)] and Yadong Song (宋亚东)[1,2]

AFFILIATIONS

[1]State Key Laboratory of Rail Transit Vehicle System, Southwest Jiaotong University, Chengdu 610031, China
[2]School of Mechanical Engineering, Xihua University, Chengdu 610031, China

[a)]Author to whom correspondence should be addressed: yyuan8848@163.com

ABSTRACT

Inside small cross section single-track tunnels, the ride comfort for drivers and passengers has been considerably impacted by the sustained lateral swaying in the tail car of the 160 km/h power-concentrated electric multiple unit (EMU). Nevertheless, previous studies have mostly focused on unilateral train aerodynamics or vehicle dynamics. Systematic investigations into the mechanisms governing fluid–structure coupling vibrations in trains inside tunnels remain insufficiently explored. Therefore, a fluid-structure coupling simulation platform for 9-car marshaling train aerodynamics and vehicle dynamics is constructed, and the accuracy and efficacy of the coupling method are validated through on-track tests. On this basis, aerodynamic loads and dynamic responses of the carbody while EMUs traverse tunnels are investigated. Furthermore, the effects of differing carbody lengths and head shapes on coupling characteristics are examined. The results indicate that the front and rear ends of the carbody are subjected to aerodynamic loads, which induce carbody lateral displacement and rotational motion. The coupling effect alters the amplitude and frequency of aerodynamic loads with aerodynamic load frequencies synchronized to carbody vibration frequencies. Harmonic vibration is obviously detected at both the front and rear ends of the carbody with the rear end exhibiting greater intensity. The aerodynamic shape of the tail car predominantly affects the intensity of aerodynamic loads. The vibration frequency of the carbody is primarily influenced by two factors: the train's running velocity and the interplay between the carbody's dynamic response and the surrounding flow field. This work can provide a reference for the aerodynamic shape optimization of trains traversing tunnels.

NOMENCLATURE

Acc	Vibration acceleration
Acc_y	Lateral vibration acceleration
Acc_z	Vertical vibration acceleration
d_1	Moment arm between F_{y1} and the center of gravity
d_2	Moment arm between F_{y2} and the center of gravity
f	Vibration frequency
$F(f)$	Frequency correction factor
F_y	Aerodynamic lateral force on the whole carbody
F_{y1}	Component of lateral aerodynamic loads at the front end of the carbody
F_{y2}	Component of lateral aerodynamic loads at the rear end of the carbody
F_z	Aerodynamic vertical force on the whole carbody
F_{z1}	Component of vertical aerodynamic loads at the front end of the carbody
F_{z2}	Component of vertical aerodynamic loads at the rear end of the carbody
H	Train height
M_x	Aerodynamic roll moment on the whole carbody
M_y	Aerodynamic pitch moment on the whole carbody
M_{y1}	Pitch moment generated by F_{z1}
M_{y2}	Pitch moment generated by F_{z2}
M_z	Aerodynamic yaw moment on the whole carbody
M_{z1}	Yaw moment generated by F_{y1}
M_{z2}	Yaw moment generated by F_{y2}
P_y	Lateral displacement of the carbody
P_z	Vertical displacement of the carbody
Re	Reynolds number

U	Incoming flow speed
W	Ride comfort index
W_y	Lateral ride comfort index
W_z	Vertical ride comfort index
θ	Pitch angle of the carbody
μ	Air dynamic viscosity
ρ	Air density
ϕ	Roll angle of the carbody
ψ	Yaw angle of the carbody

I. INTRODUCTION

Since the China Railway 200J (CR200J) power-concentrated electric multiple unit (EMU), designed for 160 km/h, commenced operations in January 2019, the lateral dynamic performance of certain EMUs significantly deteriorated while traversing small cross section single-track tunnels. The issues include the lack of hunting stability on local railways,[1–3] disparities in the lateral ride comfort index at both ends of the locomotive,[4] and the significant degradation of lateral ride comfort due to the persistent swaying of the tail car in the single-track tunnel.[5] The long and short marshaling of EMUs exhibit significant lateral vibration in the tail car while traversing single-track tunnels, resulting in discomfort for both drivers and passengers. The phenomenon occurs only inside tunnels, indicating that the vibration is induced by aerodynamic loads.

In the 1990s, Shinkansen trains in Japan exhibited lateral swaying when traversing tunnels, with the swaying amplitude progressively increasing from the front car to the tail car.[6] Extensive research has been conducted on this issue, particularly focusing on the train tail's lateral swaying behavior in tunnels. Takai[7] first posited that aerodynamic loads within the tunnel were the primary reason, while the impact of track excitation was small. Suzuki[8–10] and the Railway Technical Research Institute (RTRI) in Japan revealed that a propagation pressure disturbance (PPD) along the carbody was generated within the tunnel. This disturbance is strong enough to significantly degrade the ride comfort. Diedrichs *et al.*[11,12] used large eddy simulation (LES) to investigate the aerodynamic responses of the Japanese S300 and German ICE2 trains within a tunnel. The study indicates that flow separation induces vibrations in the tail car, leading to a linear increase in pressure disturbances from the nose to a distance of 150–200 m downstream. The vibration is associated with the aerodynamic shape and the mass of the tail car with the lateral aerodynamic force of the S300 being almost double that of the ICE2. Utilizing pressure data collected in tunnels, Tanifuji *et al.*[13] established a mathematical model to examine train ride comfort under aerodynamic loads. Choi *et al.*[14] used computational fluid dynamics (CFD) simulation to investigate the effects of head shape length and tunnel cross-sectional area on the aerodynamic drag of the train.

The impact of the train's aerodynamic shape on the wake structure is notably obvious. Wang *et al.*[15] examined the impact of the bogie structure on the train wake. The findings indicate that the bogie structure is not the primary cause of wake spanwise oscillation. The turbulent motion at the bogie initiates an early instability and propagates downstream, consequently enhancing the natural convection instability of the wake vortex pair and resulting in oscillation. Zhou *et al.*,[16] based on the proper orthogonal decomposition (POD) approach, observed that vortex pairs of the full-scale bogie train alternately falloff in the wake, which is mainly related to the vortex shedding in the bogie area. Bell *et al.*[17] analyzed the wake structure of high-speed trains at various vertex angles in a 1:10 scale wind tunnel test. The results indicated that as the vertex angle increases, the unsteady wake, initially characterized by a pair of streamwise vortices exhibiting sinusoidal asymmetry motion, progressively transforms into a large-scale unsteady separation motion. Hemida and Krajnović[18,19] investigated the influence of head shape length and yaw angle of the train on the flow field structure and aerodynamic performance. The findings indicate that the three-dimensional (3D) and transient characteristics of the flow field surrounding the short head shape are more pronounced. Additionally, more vortex structures are observed in the wake vortex.

Advancements in computer technology have significantly enhanced research on the fluid-structure coupling of trains.[20] Li *et al.*[21,22] proposed an embedded fluid-structure coupling method for high-speed trains. This method enables analysis of the interaction between the air and the carbody under the impact of crosswinds. Cui *et al.*[23] investigated the fluid-structure interaction vibrations of high-speed trains. The findings indicate that after considering the coupling, both crosswind and train crossing safety reduce further. Ji *et al.*[24] investigated the fluid-structure coupling characteristics of trains traversing tunnels while considering track excitation. The findings indicate that as the train traverses the tunnel, both lift and lateral acceleration exhibit significant variation, while the lateral vibration frequency of the carbody is primarily influenced by vertical track excitation and the carbody's natural frequency. Li *et al.*[25] studied the swaying mechanism of the tail car running in the tunnel of the 160 km/h urban EMU and analyzed the influence of vehicle suspension parameters and track excitation on the lateral swaying of the tail car. The results show that the frequency of the swaying is independent of its hunting frequency and only depends on the aerodynamic frequency acting on the tail of the train.

Vortex-induced vibration (VIV) is a classic fluid-structure interaction phenomenon caused by the interplay between fluid dynamics and an elastic system.[26,27] Currently, research on VIV focuses mainly on slender structures, including marine pipelines and long-span bridges, with significant advancements achieved.[28–30] Vortex-induced resonance occurs when the vortex-induced frequency approaches a certain natural frequency of the structure, resulting in the vortex-induced force frequency being locked with the natural frequency.[31] Yao *et al.*[5] incorporated the theory of VIV into the analysis of train wake and discovered that a frequency locking phenomenon occurs when the vortex shedding frequency approximates the lateral vibration frequency of the carbody. When the vortex shedding frequency around the tail car is close to the natural frequency of the train (such as primary hunting frequency), a more intense coupling vibration will be generated. Song *et al.*[32–34] established a fluid-structure coupling model of the EMU tail car to investigate its dynamic performance in a tunnel. These studies demonstrate that alterations in vehicle dynamic parameters substantially affect the aerodynamic loads exerted on the carbody. This finding highlights the significance of considering fluid-structure coupling when analyzing vehicle dynamics in confined environments like tunnels.

In this paper, a fluid-structure coupling simulation platform for a 9-car marshaling system within a small cross-sectional single-track tunnel is established, taking into account the effects of track excitation and the tunnel. Based on this method, this study examines the fluid-structure coupling vibration characteristics of the tail car in the tunnel and the influence of aerodynamic shapes on the coupling

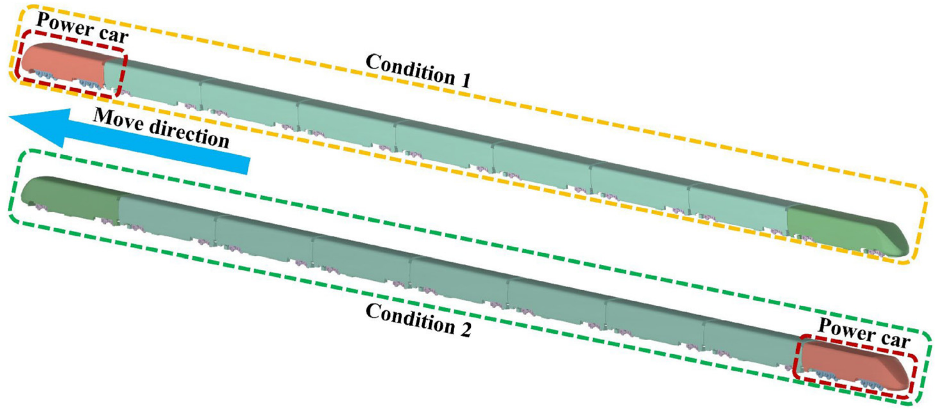

FIG. 1. On-track test under different conditions of CR200J1-D EMU.

characteristics. The structure of this paper is as follows: On-track test results are introduced in Sec. II. The train fluid-structure coupling method is introduced and verified in detail in Sec. III. The influence of carbody lengths and head shapes on fluid-structure coupling vibration of the tail car is discussed in Sec. IV. Concluding remarks are subsequently offered in Sec. V.

II. ON-TRACK TEST RESULTS

The CR200J1-D EMU is part of the third-generation CR200J series, configured as 1M8T marshaling, and is engineered for a maximum velocity of 160 km/h. The first batch of CR200J1-D EMUs is specifically engineered for the attributes of the Li Xiang railway. The Yunnan Li Xiang railway extends 140 km, featuring a design velocity of 140 km/h. It consists of 19 bridges and 20 tunnels, which together account for 73% of the railway's length. In November 2023, the dynamic response of the carbody of the CR200J1-D EMU was measured while traversing a tunnel at varying velocities. The test conditions are presented in Fig. 1 and Table I. The test comprises two conditions: condition 1 positions the power car at the front of the train, whereas condition 2 positions the power car at the rear of the train.

In this paper, the Sperling index W is used to evaluate the ride comfort of trains. The calculation process is introduced in Sec. III B 2. The test results of W_y and W_z are shown in Fig. 2. The analysis of the test data summarizes the swaying rules and features of the CR200J1-D EMU operating on the Li Xiang railway as follows:

(1) The W_y under condition 2 significantly exceeds the W_y under condition 1. The maximum W_y for the control car cab is 3.36, while that for the power car cab it is 3.00.

TABLE I. On-track test conditions.

Condition	The power car position	Velocity
Condition 1	Head of the train	100 km/h 120 km/h 140 km/h
Condition 2	Rear of the train	100 km/h 120 km/h 140 km/h

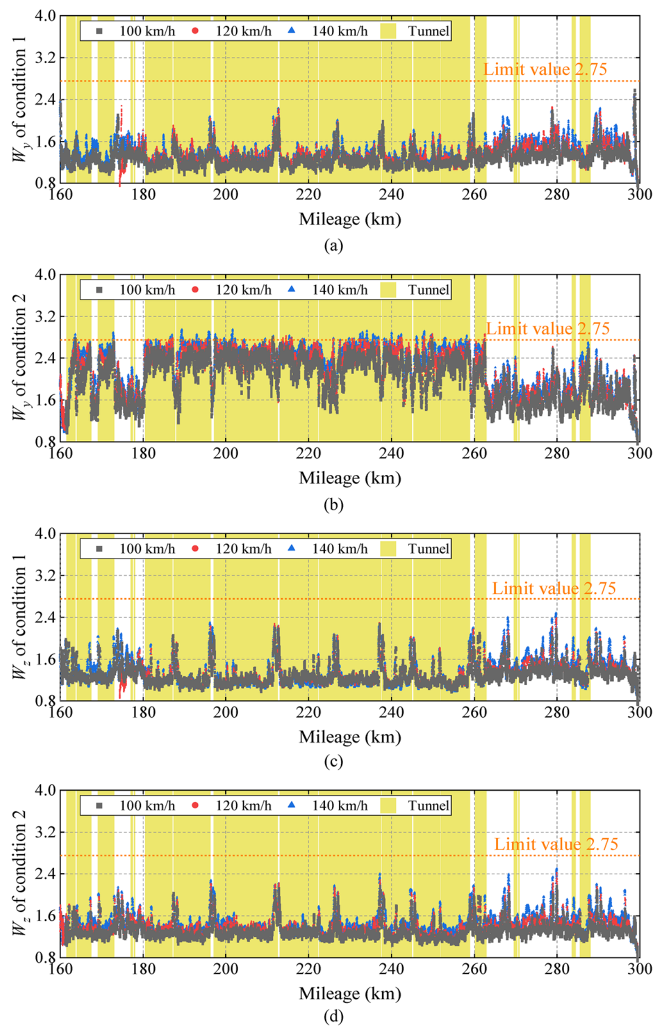

FIG. 2. The on-track test results of W of the CR200J1-D EMU power car cab under different conditions. (a) W_y of condition 1. (b) W_y of condition 2. (c) W_z of condition 1. (d) W_z of condition 2.

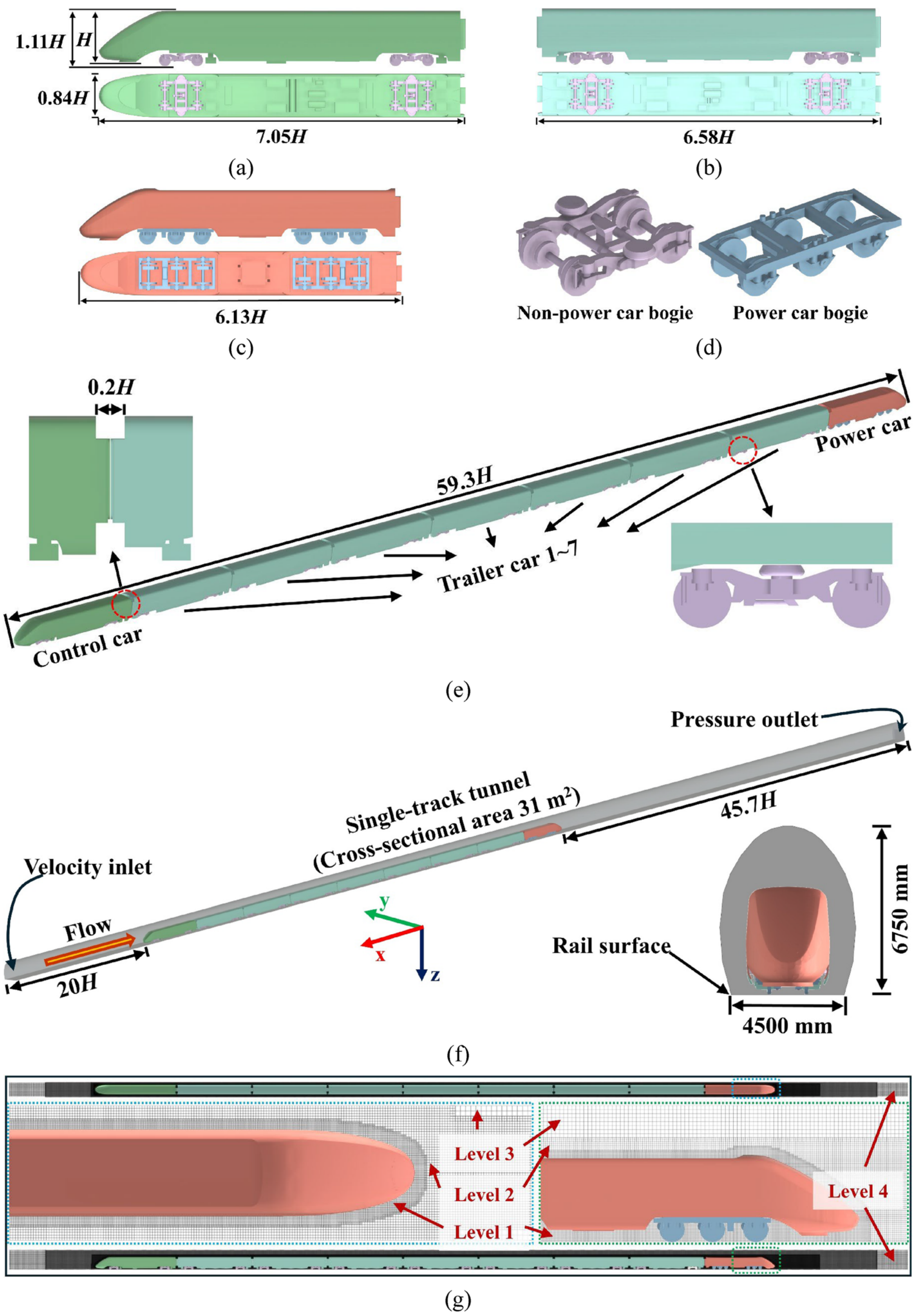

FIG. 3. Aerodynamics model of CR200J1-D EMU: (a) Control car. (b) Trailer car. (c) Power car. (d) Simplified bogie. (e) 9-car marshaling. (f) Computational domain and boundary conditions. (g) Computational particles.

(2) Under condition 2, the elevated value of the W_y primarily manifests in the tunnel section, particularly obvious when the train operates inside single-track tunnels. Harmonic vibration is apparent at both ends of the carbody inside the tunnel, although it is comparatively subdued in the center of the carbody.
(3) Under condition 2, as the velocity escalates from 100 to 140 km/h, the probability of W_y surpassing the limit value of 2.75 progressively increases.
(4) Compared to W_y, W_z shows no substantial deviation in either direction, remaining within the limit of 2.75.

III. TRAIN FLUID–STRUCTURE COUPLING VIBRATION SIMULATION PLATFORM

A. Train-tunnel aerodynamics model

The aerodynamic models are formulated using the CFD software SIMULIA XFlow. The solver employs a novel fully Lagrangian

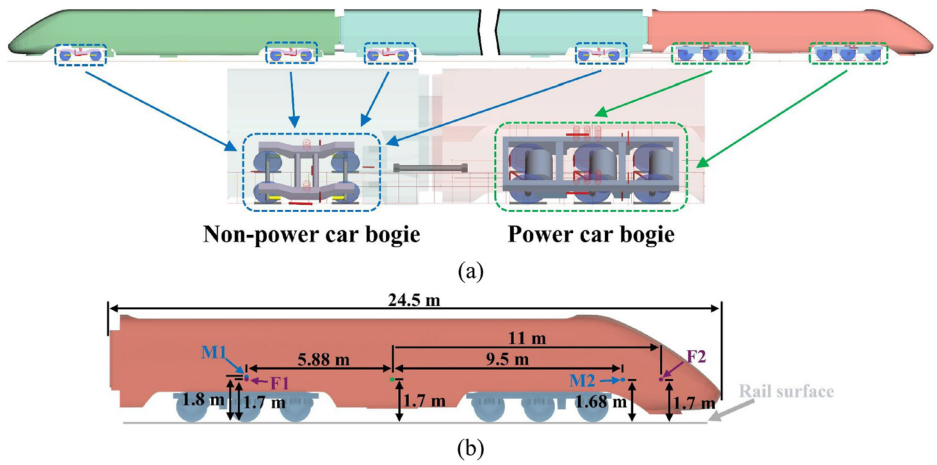

FIG. 4. EMU vehicle dynamics model: (a) 9-car marshaling and bogie structure. (b) Acceleration measuring points and aerodynamic load loading points.

particle-based kinetic approach rooted in the lattice Boltzmann method (LBM). This methodology enables computationally efficient implementation of large eddy simulation (LES) turbulence modeling. The train aerodynamics models are shown in Figs. 3(a)–3(e). The EMU consists of 1 control car, 7 trailer cars, and 1 power car, and the power car is the tail car. The head shape of both the control car and the power car is identical, with a characteristic height of $H = 4.0$ m. The model simplifies the details of pantograph, window, door, equipment at the bottom of the train and bogie, as the essential aerodynamic shape is the focus of this investigation.

TABLE II. Main dynamic parameters of the CR200J EMU.

Parameter	Value: Non-power car	Value: Power car	Unit
Carbody mass	42.91	72.65	t
Bogie frame mass	2.54	5.90	t
Wheelset mass	1.74	2.84	t
Bogie wheelbase	2.60	2.15/2.00	m
Distance between bogie centers	18.00	11.76	m
Wheel rolling circle diameter	0.915	1.25	m
Wheel profile type	LM	JM_3	/
Distance of contact point	1.493	1.493	m
Track gauge	1.435	1.435	m
Maximum operation speed	160	160	km/h

TABLE III. Frequency domain correction coefficient of *W*.

Direction	Frequency range (Hz)	Correction factor
Lateral acceleration Acc_y	$0.5 \le f < 5.4$	$0.8f^2$
	$5.4 \le f < 26$	$650/f^2$
	$f \ge 26$	1
Vertical acceleration Acc_z	$0.5 \le f < 5.9$	$0.325f^2$
	$5.9 \le f < 20$	$400/f^2$
	$f \ge 20$	1

The calculation domain and boundary conditions are shown in Fig. 3(f). The tunnel entrance is set as the velocity inlet, and the velocity increases linearly from 0 to 38.89 m/s (140 km/h) within 4 s. The tunnel exit is set as the pressure outlet, and the outlet pressure is set as 0 Pa. The length of the single-track tunnel is set to 125*H*, the nose tip of the control car is 20*H* from the tunnel entrance, and the nose tip of the power car is 46.3*H* from the tunnel exit, according to the standard EN 14067-6 (2018).[35] Per Chinese standards GB 146-2, TB 10621-2014, and TB 10003-2016,[36–38] the cross-sectional area above the rail surface of a single-track tunnel designed for a speed of 140 km/h must be no less than 31 m^2. Therefore, the width of the rail surface in the tunnel is set to 4500 mm, the tunnel height is 6750 mm, and the tunnel cross-sectional area is 31 m^2. According to Eq. (1), the Reynolds number is 7.9×10^6

$$Re = \rho UH/\mu, \tag{1}$$

where the air density ρ is 0.9096 kg/m^3 and the air dynamic viscosity μ is 17.9×10^{-6} Pa·s in Yunnan, China, at an altitude of 3000 m. The velocity U of the incoming flow is 38.89 m/s.

This study uses an octree lattice structure as the computational particle of CFD, based on the input geometries, with the D3Q27 configuration generated by XFlow. Consequently, an octree structure with four levels is established with the particle resolution being 0.1*H* at the far end (level 4) and 0.0125*H* at the train surface and wake (level 1), as illustrated in Fig. 3(g). There are a total of 2.37×10^7 computational particles. The sensitivity analysis of the particles is shown in Ref. 32, and the accuracy of these particles will be validated subsequently.

B. Vehicle multi-body dynamics model

1. Vehicle dynamics model

The dynamics models of the EMU are established by the multi-body dynamics software SIMULIA Simpack, as shown in Fig. 4(a). The main dynamic parameters are shown in Table II. The dynamics models are composed of 1 control car, 7 middle cars, and 1 power car. Different components are connected through the primary suspension and the secondary suspension, and carriages are connected through

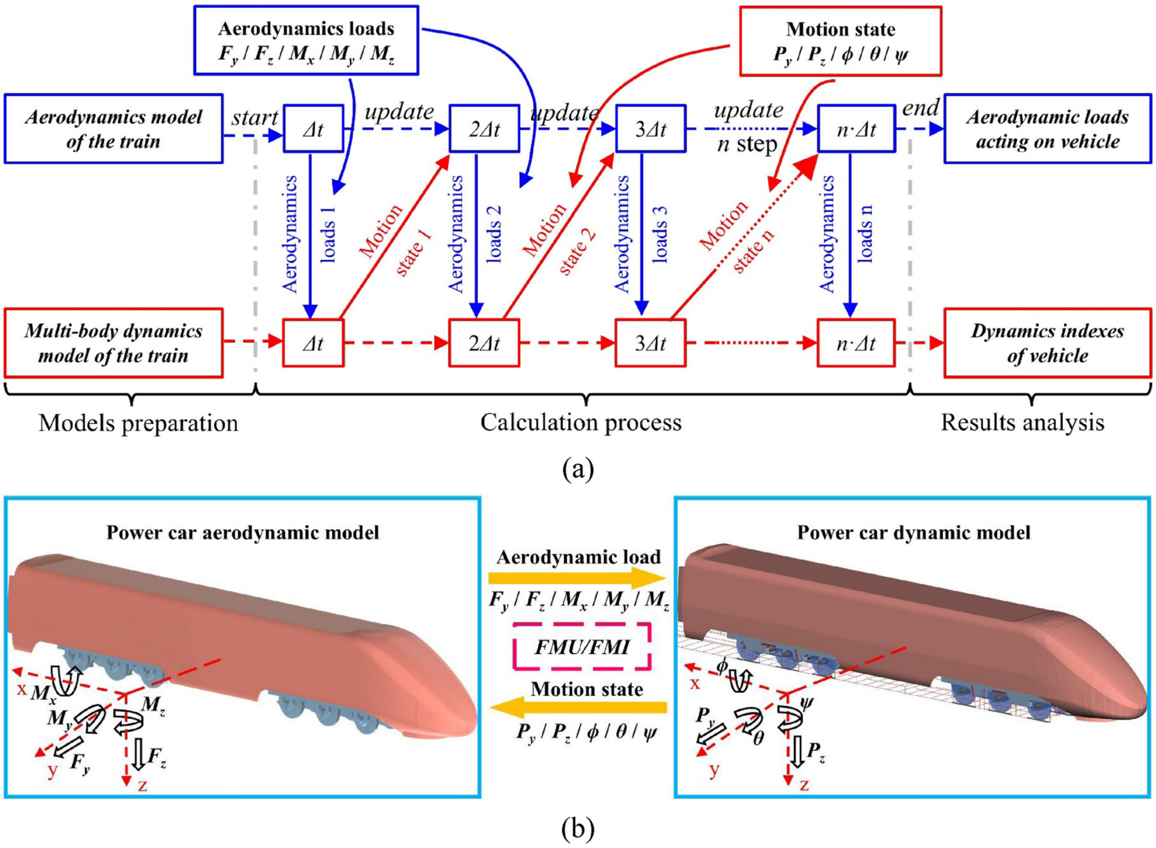

FIG. 5. The fluid-structure coupling vibration simulation model: (a) Flow chart of coupling simulation of vehicle dynamics and aerodynamic model. (b) The FMU/FMI standard interface is used to connect the aerodynamic model and the vehicle dynamics model and transmit the data.

the coupler. Additionally, the nonlinear characteristics of both the primary and secondary suspension systems are taken into account. The speed of the model is consistent with the aerodynamic model, which is 140 km/h.

Figure 4(b) shows the key point of the power car. The green point is the carbody center of gravity, which is 1.7 m in height from the rail surface. M1 is the acceleration measurement point at the carbody front end, which is located on the carriage floor surface directly above the center of the front bogie. M2 is the acceleration measurement point at the carbody rear end, which is located on the floor directly below the driver seat. F1 and F2 are the aerodynamic load loading points of the carbody. The height of F1 and F2 from the rail surface is consistent with the center of gravity. The vertical force and lateral force will be loaded on F1 and F2, and the roll moment is loaded at the carbody center of gravity. The track excitation includes lateral and vertical excitation, which is taken from a high-speed railway.

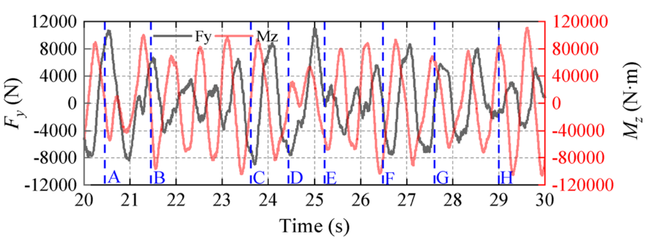

FIG. 6. Eight typical states of F_y and M_z acting on the carbody.

2. Ride comfort index

The ride comfort indices W_y and W_z are calculated as follows:[39]

TABLE IV. F_y and M_z under different states corresponding to Fig. 6.

State	Time (s)	F_y (N)	M_z (N·m)
A	20.45	8616.6	84.9
B	21.44	5869.8	−123.7
C	23.61	−7195.3	−80.5
D	24.42	−6720.4	37.7
E	25.25	−6.4	−57840.9
F	26.47	1.5	−90916.3
G	27.59	1.9	62501.7
H	28.99	−1245.8	83164.7

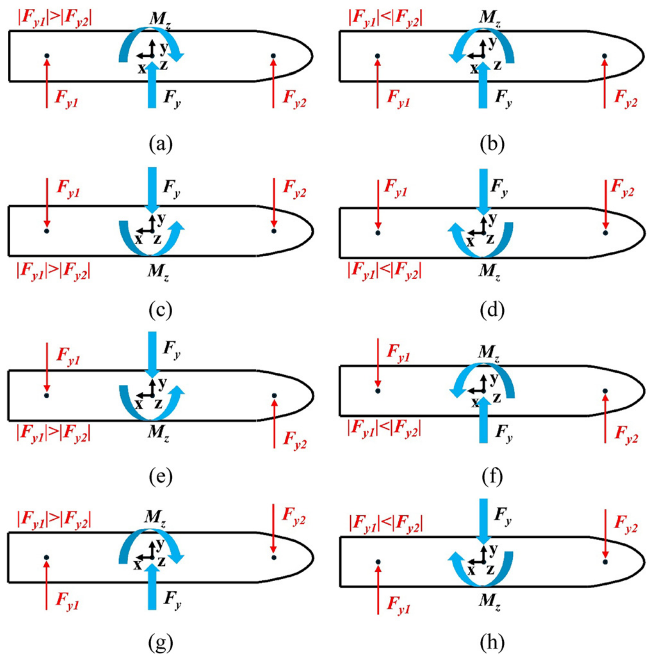

FIG. 7. Aerodynamic loads in different directions cause the car body to rotate and move laterally. These states correspond to Fig. 6 and Table IV: (a) State A. (b) State B. (c) State C. (d) State D. (e) State E. (f) State F. (g) State G. (h) State H.

$$W = 3.57\left[\frac{Acc^3}{f}F(f)\right]^{1/10}, \tag{2}$$

where a is the acceleration, f is the vibration frequency, and $F(f)$ is the frequency correction factor, indicating the sensitivity of humans to vibration. The frequency correction factor $F(f)$ is delineated in Table III. The ride comfort index W is obtained from the statistical analysis of vibration acceleration Acc with the measurement position generally situated on the carriage floor. The lesser value of W indicates superior ride comfort. The limit value for the excellent level of W in locomotives is 2.75.

TABLE V. Interpretation under different simulation methods.

Method	Interpretation
Noload	Without aerodynamic loads.
Non-coupling	Regardless of coupling, aerodynamic loads are unidirectionally loaded into vehicle dynamics models.
1-Car coupling	Train aerodynamic models and vehicle dynamics models are 9-car marshaling, but only the coupling of the tail car is considered.
9-Car coupling	Considering the coupling of all carriages in the 9-car marshaling.

C. Fluid–structure coupling method

A simulation platform for fluid–structure coupling vibration of trains in a small cross-sectional single-track tunnel is established in accordance with FMU/FMI standards. This platform employs a real-time data dynamic exchange method for simulation, as illustrated in Fig. 5, where data exchange occurs at each time step. The time steps of the two models are set to 1.8×10^{-4} s. At each time step, the lateral force F_y, vertical force F_z, roll moment M_x, pitch moment M_y, and yaw moment M_z from the aerodynamics model are conveyed to the vehicle dynamics model. Simultaneously, the lateral displacement P_y, vertical displacement P_z, roll angle ϕ, pitch angle θ, and yaw angle ψ of the vehicle dynamics model are conveyed to the aerodynamics model. In addition, the calculation time of the aerodynamic model at each time step will be much larger than that of the vehicle dynamics model. In order to avoid the time inconsistency of the two models, after the vehicle dynamics model calculates the current time step, it will wait for the aerodynamic model to calculate and transmit the aerodynamic load data of the next time step.

In the calculation of aerodynamics, aerodynamic loads are distributed across the entire carbody surface, and their effect on dynamic responses of the carbody is highly intricate. Figure 6 and Table IV illustrate that states A–H represent the eight typical states of aerodynamic loads. In states A–D, the carbody is subjected to a significant F_y and a small M_z, with aerodynamic loads inducing it to shift laterally. At states E–H, the carbody is subjected to a small F_y and a significant M_z, with aerodynamic loads inducing rotation. Consequently, in the single-track tunnel, aerodynamic loads will induce both rotation and lateral displacement of the carbody, with these two conditions potentially transforming or coexisting simultaneously.

Most existing research on vehicle dynamics applies torque or force directly to the center of the carbody. This method fails to accurately represent the lateral movement and rotation of the carbody, particularly in tunnel environments. Alternatively, aerodynamic loads are applied to the vehicle dynamics model in the form of a surface. Although this method offers higher accuracy, the calculation load is significantly large and difficult to achieve. Consequently, to minimize computational resources while maintaining result precision and to more accurately simulate the actual effects of aerodynamic loads on dynamic responses, load application points are designated at the front and rear ends of the carbody.

Taking the lateral aerodynamic loads as an example, aerodynamic loads under states A-H can be simplified as the combined effect of the lateral forces acting on the front and rear ends, as shown in Fig. 7. Furthermore, states A–H correspond one-to-one with states A–H in Fig. 6 and Table IV. In Simpack, the F_y and M_z transmitted from XFlow are decomposed using Eq. (3) to obtain the F_{y1} and F_{y2}, respectively. Likewise, the F_z and M_y are decomposed to obtain the F_{z1} and F_{z2}. Since the transverse wind condition is not considered, the M_x is negligible and thus not decomposed

$$\begin{cases} F_{y1} + F_{y2} = F_y, \\ F_{y1}d_1 - F_{y2}d_2 = M_z, \\ F_{y1} = \dfrac{F_y d_2 + M_z}{d_1 + d_2}, \\ F_{y2} = \dfrac{F_y d_1 - M_z}{d_1 + d_2}, \end{cases} \tag{3}$$

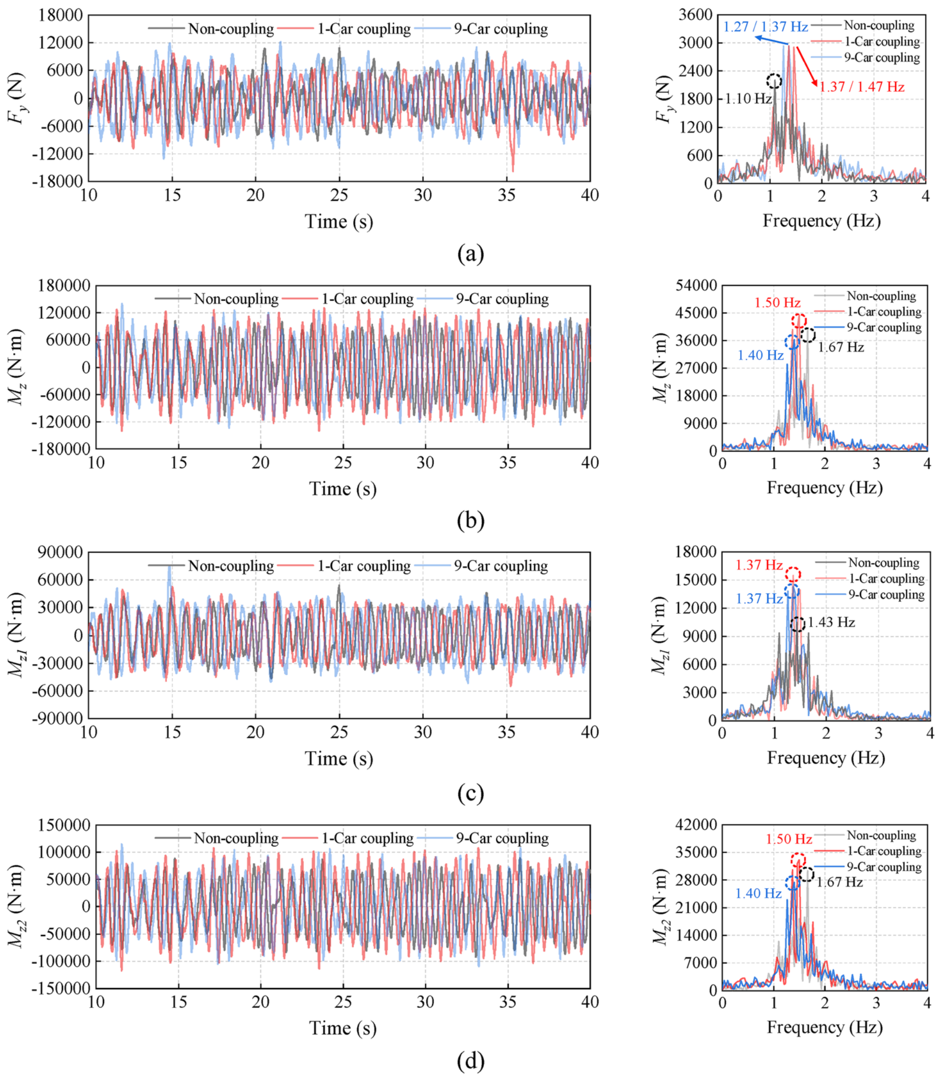

FIG. 8. Time and frequency domain of lateral aerodynamic loads under different methods: (a) F_y. (b) M_z. (c) M_{z1}. (d) M_{z2}.

where F_y is the aerodynamic lateral force. M_z is the yaw moment. F_{y1} and F_{y2} are the resolved components of lateral aerodynamic loads. d_1 is the moment arm between F_{y1} and the carbody center of gravity. d_2 is the moment arm between F_{y2} and the carbody center of gravity.

To compare results of whether to consider the coupling, four simulation methods are established, as illustrated in Table V. The lateral aerodynamic loads on the power car are shown in Fig. 8. After the fluid-structure coupling, the size and dominant frequency of F_y and M_z are altered. Under non-coupling, the dominant frequency of M_z is 1.67 Hz; with 1-car coupling, the frequency is 1.50 Hz; and with 9-car coupling, the frequency is 1.40 Hz. Due to the disparity in the force arm distance between aerodynamic load points and the center of gravity, F_{y1} and F_{y2} are transformed into the yaw moments M_{z1} and M_{z2}. M_{z2} is significantly greater than M_{z1}. The cause is that the turbulent motion at the EMU front's bogie creates an initial instability that propagates downstream. When turbulence reaches the tail car, the aerodynamic loads are initially generated at the front end. As it propagated to the nose tip, it amplifies the natural convection instability of the wake vortex pair, exacerbating the motion intensity of the wake vortex pair[15,40] and resulting in more pronounced aerodynamic loads.

Under non-coupling, the dominant frequencies of M_{z1} and M_{z2} are 1.43 and 1.67 Hz, respectively; with 1-car coupling, the frequencies are 1.37 and 1.50 Hz, respectively; with 9-car coupling, the frequencies are 1.37 and 1.40 Hz, respectively. Furthermore, after the fluid-structure coupling, the frequencies of M_{z1} and M_{z2} exhibit a tendency to align. The vertical aerodynamic loads on the carbody are illustrated in Fig. 9. M_{y2} is significantly larger than M_{y1}, and both exert a lift effect on the carbody.

Aerodynamic loads obtained from the non-coupling are applied unidirectionally to the vehicle dynamics model to obtain dynamic responses. It is compared with results obtained under conditions devoid of aerodynamic loads and coupling. As illustrated in Figs. 10(a) and 10(b), there is a distinct harmonic vibration at both ends, with the vibration intensity at the rear end being greater. In the absence of aerodynamic load, the dominant frequencies of the front end's Acc_y are

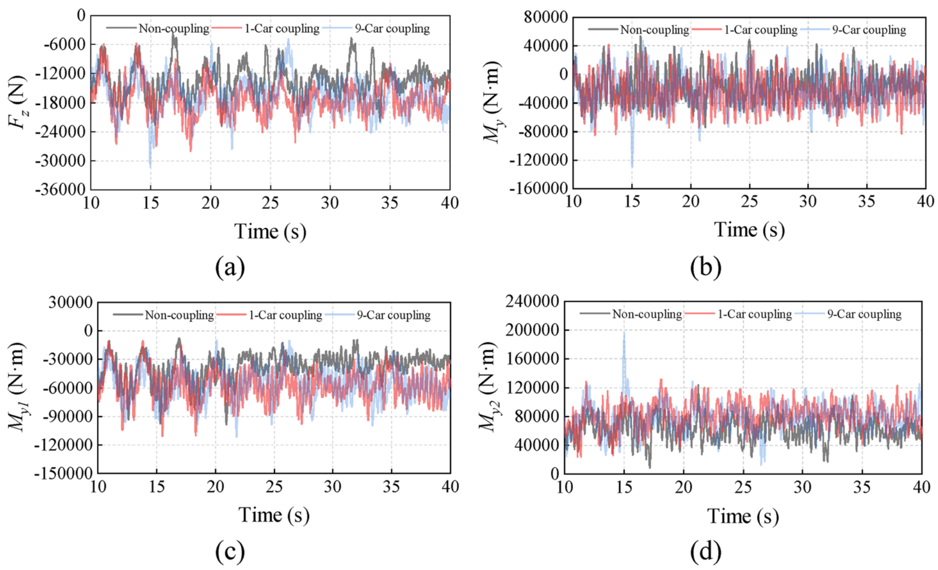

FIG. 9. Time domain of vertical aerodynamic loads under different methods: (a) F_z. (b) M_y. (c) M_{y1}. (d) M_{y2}.

0.57 and 1 Hz, while the dominant frequencies of the rear end's Acc_y are 0.8 and 1 Hz. When the coupling is not considered, the dominant frequency of the front end's Acc_y is 1.1 Hz, and the dominant frequency of the rear end's Acc_y is 1.67 Hz. After 1-car coupling, the dominant frequency of the front end's Accy is 1.47 Hz, and the dominant frequency of the rear end's Accy is 1.50 Hz. After 9-car coupling, the dominant frequency of both ends is 1.37 Hz, which is nearer to the frequency observed without aerodynamic loads.

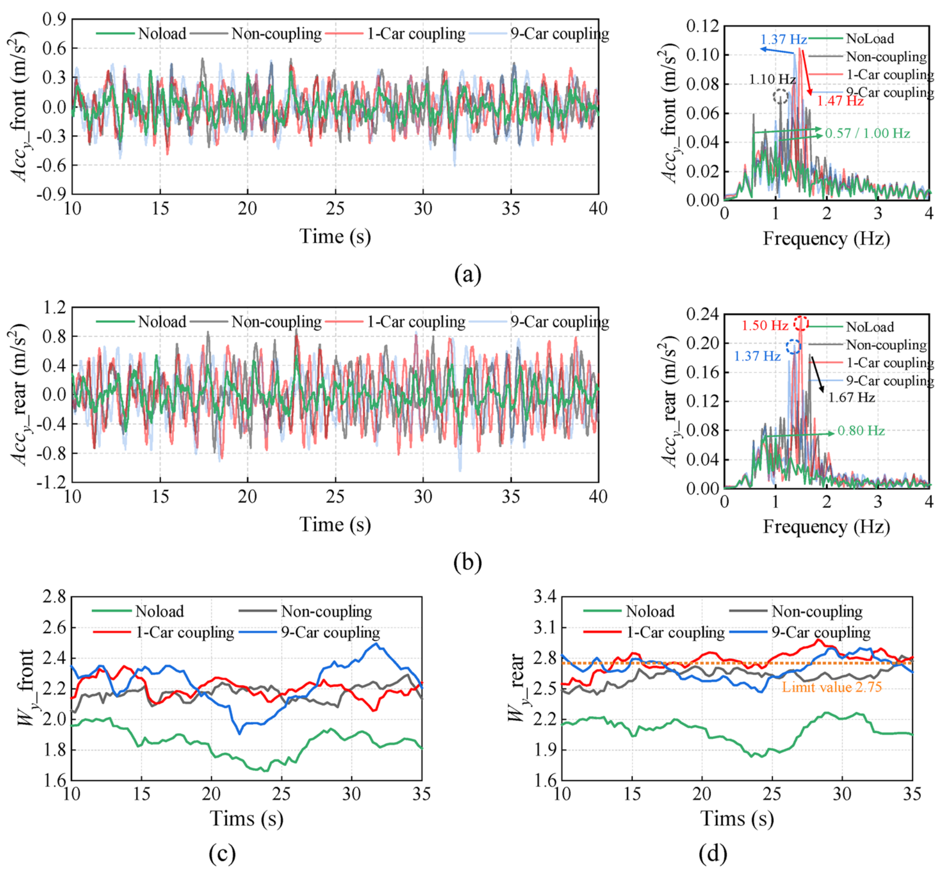

FIG. 10. At the speed of 140 km/h, the time domain and frequency domain results of Acc_y and W_y under different methods are compared. (a) Acc_y at the front end. (b). Acc_y at the rear end. (c) W_y at the front end. (d) W_y at the rear end.

TABLE VI. Statistics of W_y under different methods.

Position	Method	Maximum	Minimum	Average
Front end	Noload	2.01	1.66	1.85
	Non-coupling	2.29	2.04	1.91
	1-Car coupling	2.35	2.06	2.20
	9-Car coupling	2.50	1.91	2.24
Rear end	Noload	2.27	1.83	2.10
	Non-coupling	2.82	2.44	2.63
	1-Car coupling	2.98	2.53	2.78
	9-Car coupling	2.90	2.47	2.70

Figures 10(c) and 10(d) and Table VI present the W_y under different methods. The fluid-structure coupling can alter the magnitude and frequency of aerodynamic loads, thereby influencing dynamic responses. Furthermore, the results of 1-car coupling and 9-car coupling are significantly different. Under 9-car coupling, the vibration frequency is lower, and the W_y is smaller. Concurrently, the W_y variation trend of the 9-car coupling and non-aerodynamic loads exhibits similarity. These indicate that the flow field surrounding the tail car is affected by the motion of the front carriage, consequently influencing the dynamic response of the tail car.

D. Verification of the coupling method

Figure 11 and Table VII illustrate the results of the power car cab under on-track test and simulations. Test 1 and test 2 are on-track test results of EMU operating in different straight tunnels of the Li Xiang railway, in which the entering and leaving tunnel states are excluded. Both the test and simulation velocities are 140 km/h. The simulation results align with the test results, despite some variations. The differences are mostly attributed to the inability of the simulation circumstances to accurately emulate the test conditions, including model simplification, track excitation, track elastic deformation, random wind, and several other stochastic interference causes. Comparing different coupling methods, it is found that the results of 9-car coupling are closer to the results of on-track test on the vibration dominant frequency and the average of the lateral ride comfort index. In addition, the 9-car coupling method is closer to the actual operation of the train, so the 9-car coupling method is used for this research.

Furthermore, the amplitude of the Acc_z is greatly reduced compared to the Acc_y, and the main frequency range is 1.10–1.60 Hz. This finding suggests that aerodynamic loads in the tunnel predominantly impact the lateral dynamics performance, exerting no influence on the vertical. This difference can be ascribed to the lift being considerably lower than its weight of 72.68 t.

Aerodynamic loads and dynamic response of the carbody are significantly influenced by the coupling effect. Meanwhile, results of the coupling simulation align well with on-track test, indicating that

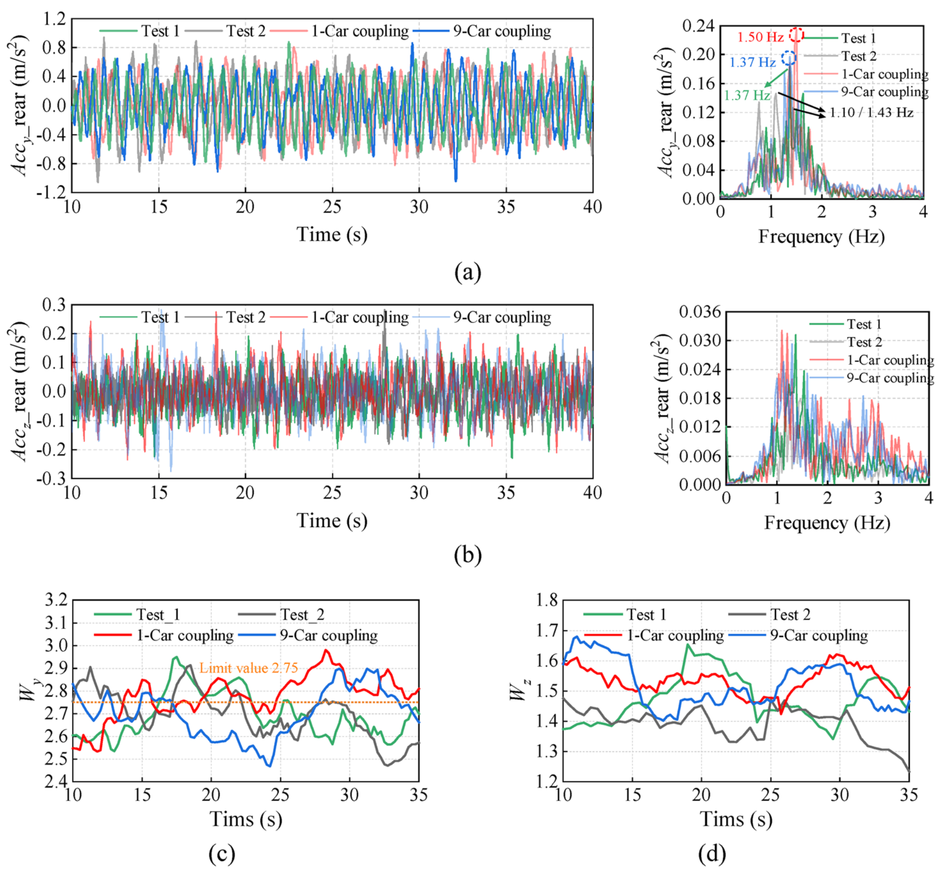

FIG. 11. At the speed of 140 km/h, the time and frequency domain of *Acc* and *W* of the power car cab under on-track test and simulation are compared: (a) Acc_y. (b) Acc_z. (c) W_y. (d) W_z.

TABLE VII. Statistics of W at carbody rear end under test and simulation.

Ride comfort index	Condition	Maximum	Minimum	Average
W_y	Test_1	2.95	2.54	2.69
	Test_2	2.91	2.47	2.70
	1-Car coupling	2.98	2.53	2.78
	9-Car coupling	2.90	2.47	2.70
W_z	Test_1	1.65	1.34	1.47
	Test_2	1.48	1.23	1.39
	1-Car coupling	1.62	1.42	1.53
	9-Car coupling	1.68	1.40	1.52

computational particles are both effective and accurate. This underscores the unique benefits of the coupling method in examining train VIV in small cross section tunnels.[32–34] Therefore, subsequent research employs the fluid-structure coupling method, exclusively focusing on the lateral dynamic response.

IV. RESULTS AND DISCUSSION

In Sec. III, the simulation and test results demonstrate that, in the small cross section single-track tunnel, the sustained lateral swaying of the tail car is attributable to excessive aerodynamic loads. Altering and optimizing the tunnel on the constructed railway is fundamentally infeasible. Consequently, the optimization of either aerodynamics or vehicle dynamics performance of the train is essential to mitigate the effects of fluid-structure coupling vibrations. This section examines the potential impact of aerodynamic shapes on aerodynamic loads without changing the vehicle dynamics model, offering a reference for mitigating the coupling vibration of the carbody.

A. Carbody length

The train aerodynamics models illustrated in Fig. 12 feature a constant head shape, with three distinct carbody lengths of 20.2, 24.5, and 28.2 m established. These lengths are derived from various standard carbody lengths of the CR200J EMU. Meanwhile, the bogie spacing is modified to accommodate the differing carbody lengths. Furthermore, in the vehicle dynamics model, as the carbody length changes, the suspension parameters remain constant, and only the locations of the acceleration measurement points and aerodynamic load points are adjusted.

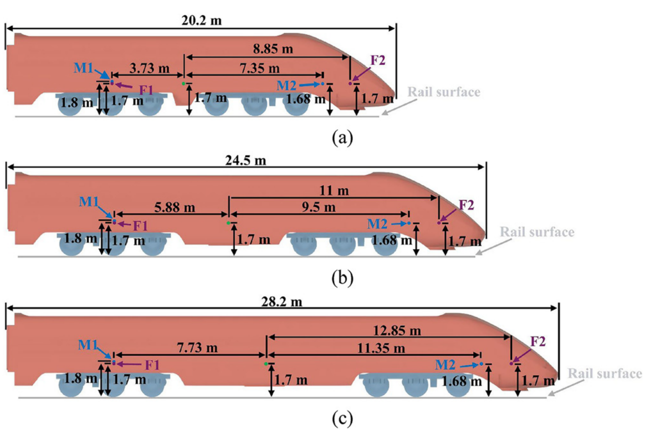

FIG. 12. Numerical simulation model of different carbody length: (a) 20.2 m. (b) 24.5 m. (c) 28.2 m.

Figures 13(a) and 13(b) illustrate the variations in F_y and M_z for different carbody lengths. As the carbody length extends from 20.2 m to 28.2 m, the amplitude of M_z escalates from 92.3 to 155.6 kN·m, reflecting a rise of 68.58%, whereas F_y diminishes. Figures 13(c)–13(e) illustrate that as the carbody length expands, both M_{z1} and M_{z2} exhibit an upward trend. F_{y2} remains relatively stable, fluctuating primarily within ± 9 kN, as shown in Fig. 13(f). As the carbody length increases, the force arm d_2 of F_{y2} relative to the carbody's center of gravity rises from 8.85 to 12.85 m, resulting in an increase in M_{z2}. The same applies to M_{z1}.

The turbulent motion produced by the front part of the EMU propagates downstream to the front end of the tail car, where it initially induces aerodynamic loads. Subsequently, these turbulences propagate from the front end to the rear and ultimately shed from the nose tip, thereby affecting the rear end. The time difference between aerodynamic loads at the front and rear ends induces a phase difference. A clear phase difference between the M_{z1} and M_{z2} peak points is visible in the 20.2 m carbody. This indicates that, at certain instances, M_{z1} and M_{z2} may cancel each other out. This situation resembles that depicted in Figs. 7(a)–7(d), that is, F_{y1} and F_{y2} are in the same direction. As a result, the carbody is subjected to a larger F_y and a smaller M_z. As the carbody length increases from 20.2 to 28.2 m, the time required for turbulence to propagate from the front to the rear increases, resulting in a rightward shift of the M_{z2} curve and a reduction in the phase difference between M_{z1} and M_{z2}. This indicates that, at certain instances, M_{z1} and M_{z2} may superimpose each other out. This situation resembles that illustrated in Figs. 7(e)–7(h), wherein F_{y1} and F_{y2} are oriented in opposing directions. As a result, the carbody is subjected to a smaller F_y and a larger M_z.

This finding clarifies the results shown in Fig. 14, where the 20.2 m carbody exhibits a greater lateral displacement, whereas the 28.2 m carbody exhibits a larger yaw angle. Moreover, alterations in carbody length do not affect the frequency of lateral aerodynamic loads, which remains within the range of 1.33–1.40 Hz.

Figures 15(a) and 15(b) illustrate the Acc_y. As the carbody length expands from 20.2 to 28.2 m, aerodynamic loads increase, concurrently resulting in a rise in Acc_y. The dominant frequency of Acc_y is unaffected by carbody length, aligning with the aerodynamic load frequency of around 1.37 Hz. It is speculated that there are two main reasons. On the one hand, the high wind speed surrounding the train renders the turbulence propagation time virtually unaffected by variations in carbody length. On the other hand, when the coupling effect is considered, VIV occurs,[32–34] with the vortex shedding frequency and the vibration frequency locked at 1.37 Hz, and the alteration in carbody length is insufficient to disrupt this locked condition.

The W_y for various carbody lengths is illustrated in Figs. 15(c) and 15(d) and Table VIII. As the carbody length increases from 20.2 to 28.2 m, the W_y gradually deteriorates. This rule aligns with the on-track test results in Sec. II, indicating that W_y exceeds the power car when the 28.2 m control car serves as the tail car. Furthermore, the disparity in W_y between the front and rear ends of the 20.2 m carbody is diminished. This suggests that the short carbody can more efficiently

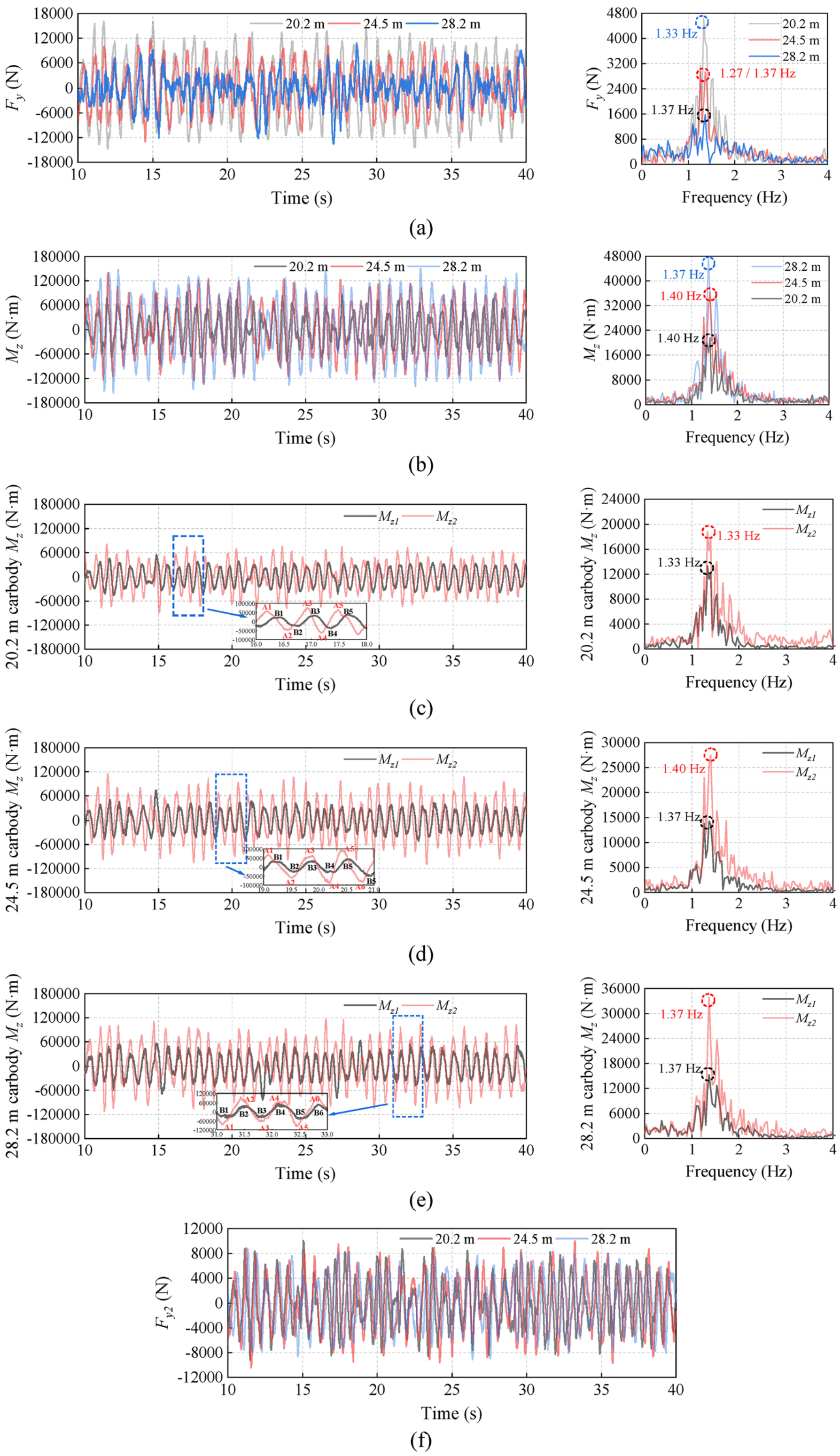

FIG. 13. Time and frequency domain of lateral aerodynamic loads under different carbody lengths: (a) F_y. (b) M_z. (c) M_{z1} and M_{z2} of 20.2 m carbody. (d) M_{z1} and M_{z2} of 24.5 m carbody. (e) M_{z1} and M_{z2} of 28.2 m carbody. (f) F_{y2}.

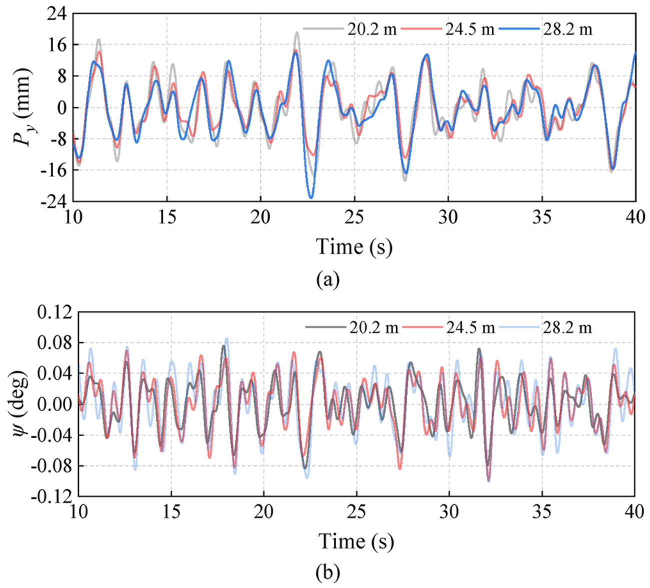

FIG. 14. The dynamic response at the carbody center of gravity: (a) Lateral displacement. (b) Yaw angle.

equilibrate the W_y between the front and rear ends. Furthermore, the W_y of 20.2 m carbody is consistently below the limit value of 2.75, and the lateral ride comfort is excellent, indicating that the shorter carbody length can significantly reduce aerodynamic loads, thus enhancing lateral ride comfort.

B. Head shape

This section examines the influence of the EMU's head shape on aerodynamic loads and lateral ride comfort. The EMU's initial head shape features a streamlined design, with a streamlined nose length (SNL) of 5.4 m. To examine the impact of differing SNLs, the SNL is adjusted to 3.4 and 9.4 m, respectively, while the overall carbody length remains at 24.5 m, as illustrated in Figs. 16(a)–16(c). Moreover, to preserve the integrity of the streamlined profile due to the larger bogie size, the bogie spacing is slightly reduced for the 9.4 m SNL. Similarly, in the vehicle dynamics model, the suspension parameters remain unchanged.

In addition, high-speed EMUs in some countries adopt non-streamlined two-dimensional (2D) plane head shapes. To explore the differences in aerodynamic characteristics between non-streamlined 2D plane head shapes and streamlined 3D head shapes inside a tunnel environment, the original EMU head shape is modified to a 2D planar form, with head shape lengths set at 5.4 and 0.9 m, respectively, as shown in Figs. 16(d) and 16(e).

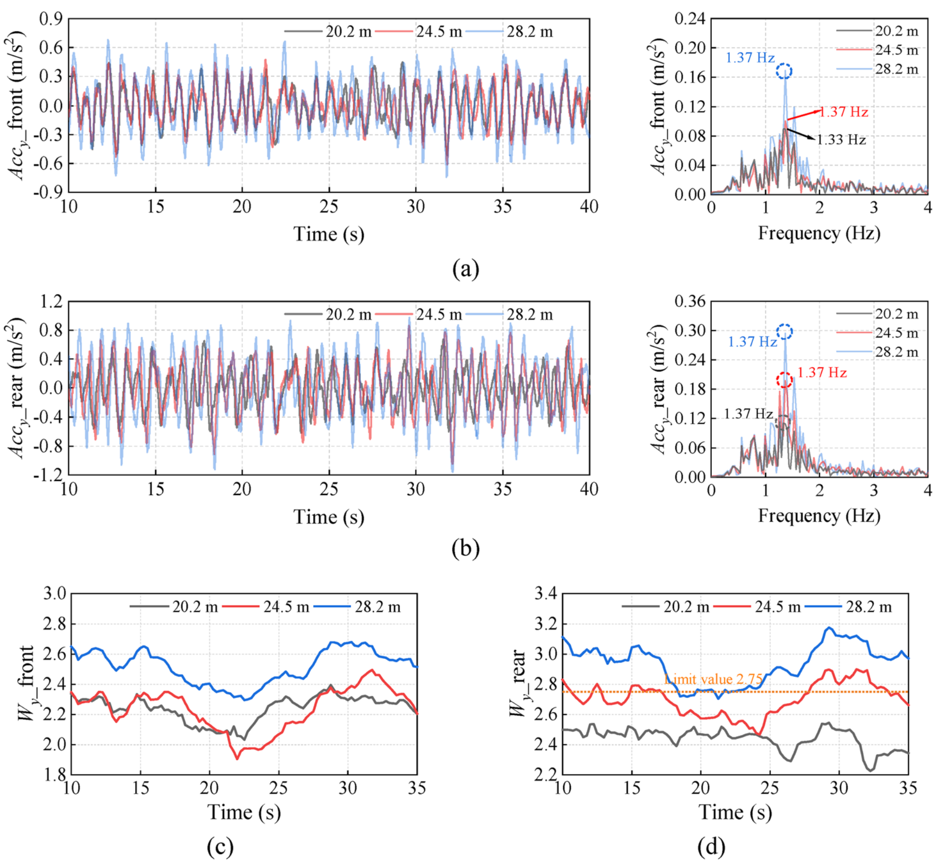

FIG. 15. Time and frequency domain of Acc_y and W_y under different carbody lengths: (a) Acc_y at front end. (b) Acc_y at rear end. (c) W_y at front end. (d) W_y at rear end.

TABLE VIII. Statistics of W_y under different carbody lengths.

Position	Carbody length	Maximum	Minimum	Average
Front end	20.2 m	2.40	2.03	2.24
	24.5 m	2.50	1.91	2.24
	28.2 m	2.68	2.30	2.52
Rear end	20.2 m	2.55	2.23	2.44
	24.5 m	2.90	2.47	2.70
	28.2 m	3.18	2.71	2.93

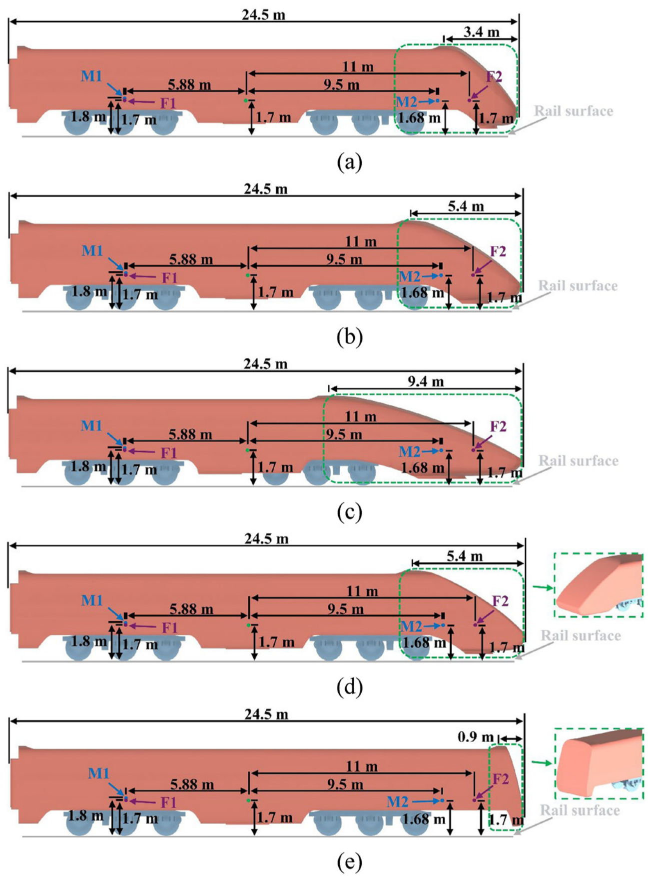

FIG. 16. Power cars with different head shapes: (a) 3.4 m SNL. (b) 5.4 m SNL. (c) 9.4 m SNL. (d) 5.4 m 2D head shape. (e) 0.9 m 2D head shape.

1. Streamline head shape

Lateral aerodynamic loads for various SNLs are presented in Fig. 17. The rise in SNL exerts a little effect on M_{z1}, whereas the amplitude of M_{z2} gradually reduces. As SNL increases from 3.4 to 9.4 m, the amplitude of M_{z2} decreases from 142.6 to 87.1 kN·m, reflecting a reduction of 38.92%. The alterations in SNL do not substantially influence the frequency of aerodynamic loads, with the dominant frequency remaining within the range of 1.27–1.4 Hz.

The Acc_y of various SNLs are illustrated in Figs. 18(a) and 18(b). SNL exerts minimal influence on the Acc_y at the front end, with the acceleration reaching the maximum value at 0.6 m/s^2. Conversely, the impact of SNL on the rear end is more pronounced. As SNL increases from 3.4 to 9.4 m, the amplitude of Acc_y at the rear end decreases from 1.046 to 0.868 m/s^2, reflecting a reduction of 17.01%. Furthermore, the dominant vibration frequency remains consistently around 1.37 Hz.

Figures 18(c) and 18(d) and Table IX provide the W_y under various SNLs. The W_y at the front end ranges from 1.9 to 2.5. The W_y at the rear end is markedly affected by the SNL. As SNL rises from 3.4 m to 9.4 m, the maximum value of W_y decreases from 3.12 to 2.75, and the average value of W_y decreases from 2.87 to 2.57, indicating reductions of 11.86% and 10.45%, respectively. Furthermore, the W_y of 9.4 m SNL is consistently below the limit value of 2.75, and the lateral ride comfort is excellent, indicating that the longer SNL can significantly reduce aerodynamic loads on the rear end of the carbody, thus enhancing lateral ride comfort.

Figure 19 illustrates the wake vortex structure identified by the Q-criterion for different SNLs. At these specific times, t = 36.08 s of 3.4 m SNL, t = 33.24 s of 5.4 m SNL, and t = 18.08 s of 9.4 m SNL, the rear end is subjected to the maximum M_{z2} in the same direction. As the Q increases, the high-vorticity layer covering the nose tip surface becomes more distinct, while vortices with lower vorticity gradually disappear. With the SNL increasing, the density and intensity of vortices covering the head shape decrease. The wake vortex structure of the 3.4 m SNL is composed of large-scale vortices with high vorticity, accompanied by a multitude of smaller-scale vortices. In contrast, the size of large-scale vortices of 9.4 m SNL is larger, the vorticity is lower, and the number of small-scale vortices is less. This comparison reveals that the vortex shedding of the short SNL is more intense, which also explains why aerodynamic loads on the rear end increase as the SNL decreases.

2. Non-streamlined head shape

Figure 20 presents the lateral aerodynamic loads for 2D and 3D head shapes. The M_{z2} of the 3D head shape slightly increases compared to that of the 2D head shape, while the phase difference between adjacent peaks of M_{z1} and M_{z2} for the 2D head shape is relatively smaller than for the 3D head shape. This results in the M_z of the 2D head shape exceeding that of the 3D head shape at certain times. The dominant frequency of aerodynamic loads remains consistent at approximately 1.37 Hz. Additionally, alterations in the length of the 2D head shape exert a negligible effect on aerodynamic loads, contrasting sharply with the effect of SNL on 3D head shapes. This indicates that the streamlining profile of the head shape's side is the primary factor affecting aerodynamic loads.

Figures 21(a) and 21(b) present the Acc_y for 2D and 3D head shapes. At certain moments, the Acc_y at the rear end of the 2D head shape is slightly higher compared to the 3D head shape. The dominant frequency remains consistent at approximately 1.37 Hz. Figures 21(c) and 21(d) and Table X illustrate the W_y of the carbody. The W_y of the 2D head shape exceeds that of the 3D head shape, suggesting that the 2D head shape is not conducive to the lateral ride comfort of the rear end.

V. CONCLUSIONS

In this paper, the accuracy of the fluid-structure coupling method of train aerodynamics and vehicle dynamics has been verified. Studies

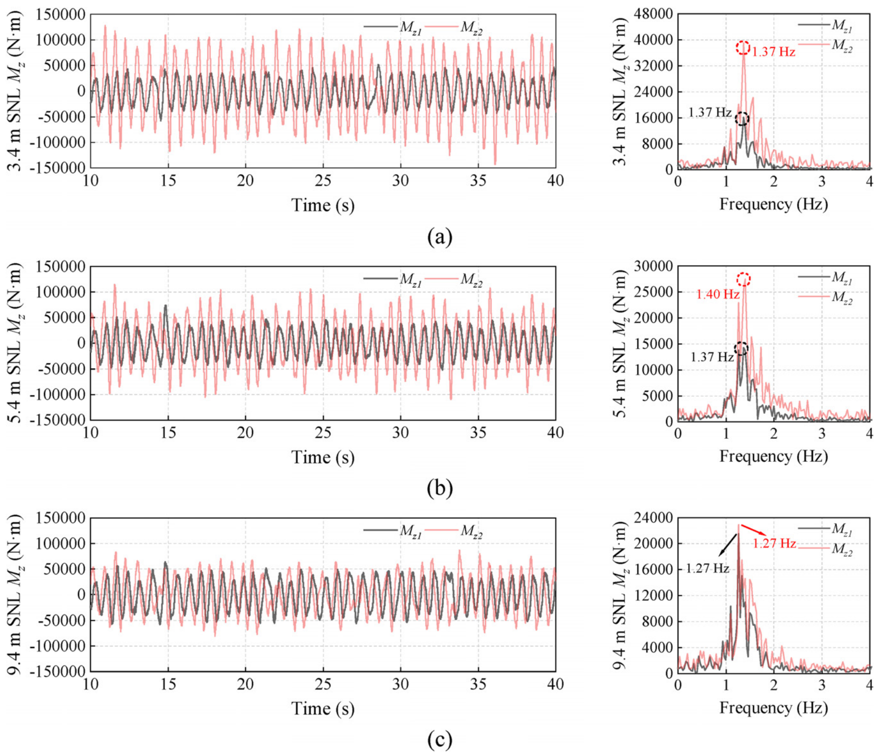

FIG. 17. Time and frequency domain of lateral aerodynamic loads under different SNLs: (a) M_{z1} and M_{z2} of 3.4 m SNL. (b) M_{z1} and M_{z2} of 5.4 m SNL. (c) M_{z1} and M_{z2} of 9.4 m SNL.

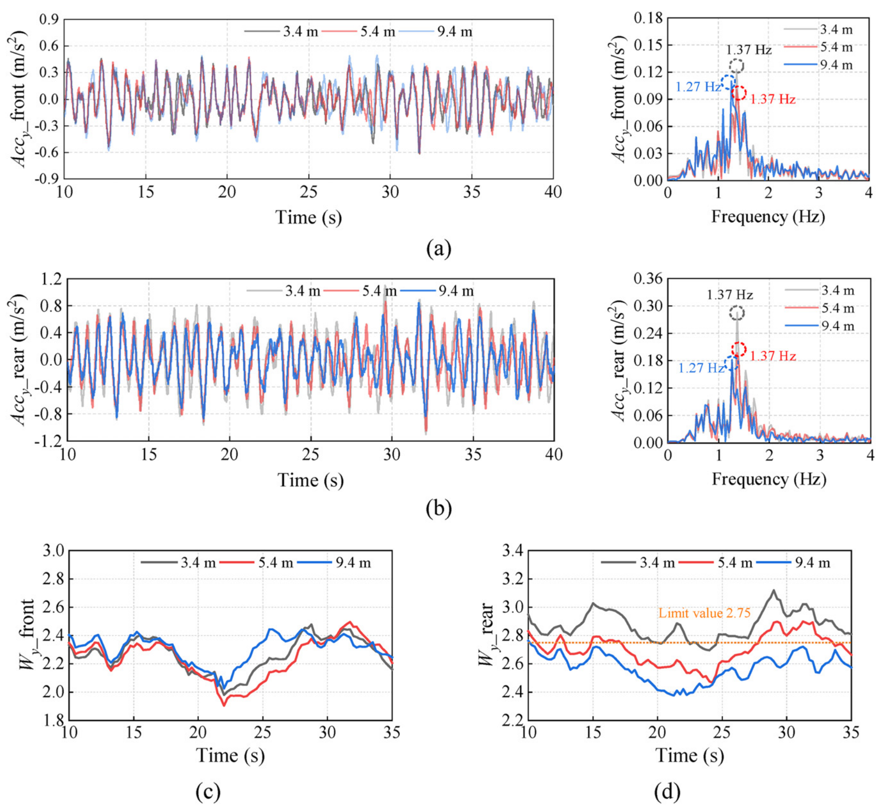

FIG. 18. Time and frequency domain of Acc_y and W_y under different SNLs: (a) Acc_y at front end. (b) Acc_y at rear end. (c) W_y at front end. (d) W_y at rear end.

TABLE IX. Lateral ride comfort index statistics under different SNLs.

Position	SNL	Maximum	Minimum	Average
Front end	3.4 m	2.48	1.98	2.26
	5.4 m	2.50	1.91	2.24
	9.4 m	2.44	2.03	2.31
Rear end	3.4 m	3.12	2.70	2.87
	5.4 m	2.90	2.47	2.70
	9.4 m	2.75	2.38	2.57

on the aerodynamic loads and carbody dynamic responses of the tail car when the EMU passes through the small cross section single-track tunnel have been conducted. Moreover, the impacts of varying carbody lengths and head shapes on aerodynamic loads and carbody dynamic responses have been examined. The results indicate the following:

(1) The turbulence generated by the bogie at the EMU's front propagates downstream, first inducing aerodynamic loads on the front end of the carbody. It then continues to propagate to the nose tip, where it amplifies the natural convection instability of the wake vortex pair, thereby increasing the aerodynamic load there. Considering the coupling effects, the amplitude of aerodynamic loads increases, and its dominant frequency becomes locked with the carbody response frequency. Both the carbody front and rear ends exhibit significant harmonic vibrations, and the vibration at the rear end is particularly intense.

(2) The time difference in the propagation of turbulence from the front end to the rear end of the carbody results in a phase difference. As the carbody length increases from 20.2 to 28.2 m, the force arm of aerodynamic loads expands. Meanwhile, the time of turbulence flowing from the front to the rear end increases, resulting in a gradual reduction of the phase difference between M_{z1} and M_{z2}, which together increases M_z by 68.58% and the average of W_y by 20.08%. The lateral displacement of the short carbody is greater, and the yaw angle of the long carbody is more pronounced. Moreover, for the long carbody, the difference in lateral ride comfort between the front and rear ends increases.

(3) As the SNL increases from 3.4 to 9.4 m, the size of the large-scale vortex within the wake structure increases, while the quantity of accompanying small-scale vortices decreases, and the vortex strength declines. Consequently, the M_{z2} decreases by 38.92%, and the average of W_y at the rear end decreases by 10.45%, enhancing the lateral ride comfort of the rear end. In comparison to the 3D head shape, the 2D head shape slightly increases aerodynamic loads and deteriorates the lateral ride comfort of the rear end. The aerodynamic loads are not basically influenced by the length of the 2D head shape. This suggests that the aerodynamic loads are primarily associated with the streamlining profile of the head shape's side.

(4) The shorter carbody combined with a longer SNL can significantly reduce aerodynamic loads. However, this configuration

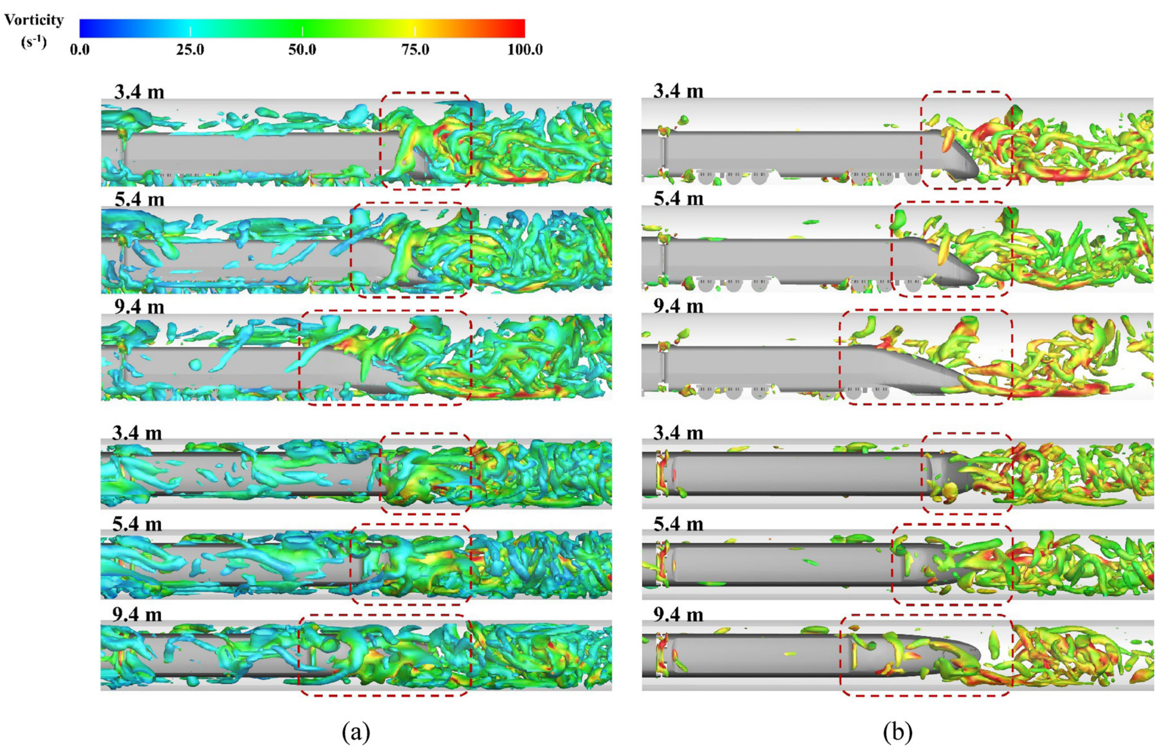

FIG. 19. Transient iso-surface corresponding to the Q criterion around the tail train: (a) $Q = 0.005$. (b) $Q = 0.05$.

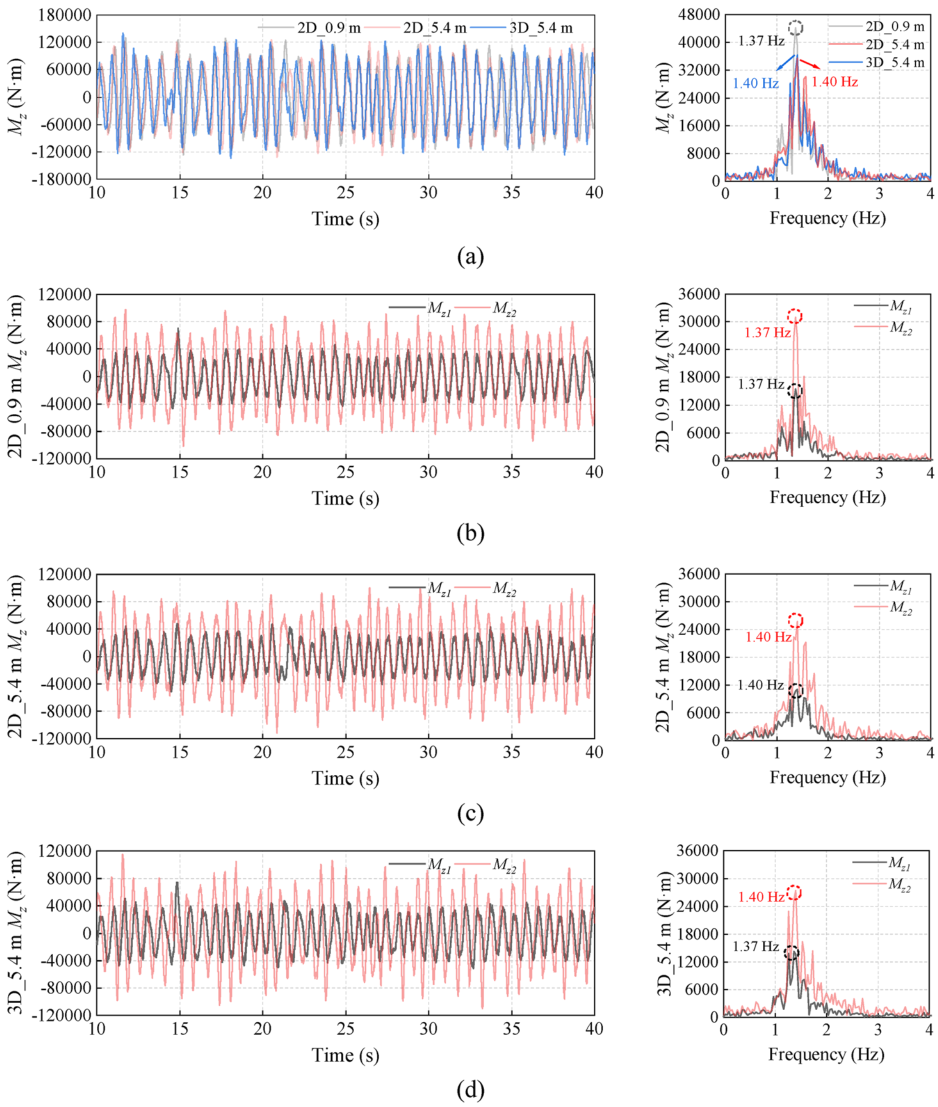

FIG. 20. Time and frequency domain of lateral aerodynamic loads under 2D and 3D head shapes: (a) M_z. (b) M_{z1} and M_{z2} of 0.9 m 2D head shape. (c) M_{z1} and M_{z2} of 5.4 m 2D head shape. (d) M_{z1} and M_{z2} of 5.4 m 3D head shape.

also has notable drawbacks. Specifically, a shorter carbody and longer SNL will compress the equipment room area of the power car and reduce the seating capacity in the control car, which is unfavorable for the operational efficiency of the EMU. Therefore, it is crucial to select an appropriate carbody length and SNL for EMUs. This balance ensures optimal aerodynamic performance and ride comfort while maximizing operational efficiency and passenger capacity.

(5) After considering the fluid-structure coupling, the variation trend of W_y remains basically consistent under varying carbody lengths and head shapes, both with and without aerodynamic loads. Additionally, the dominant frequency of aerodynamic loads and lateral dynamic responses is sustained at 1.37 Hz. The aerodynamic shape of the tail car primarily affects the magnitude of aerodynamic loads. Dynamic responses and vibration frequency are primarily influenced by two factors: the train's running velocity and the interaction between the carbody's dynamic response and the surrounding flow field. Consequently, the fluid-structure coupling method can enhance precision and more accurately replicate the actual vehicle dynamic responses in the examination of vehicle dynamics under severe aerodynamic conditions.

This research offers essential insights into aerodynamic loads and dynamic responses of the tail car inside single-track tunnels, thereby providing a more dependable foundation for the design of the train's aerodynamic shape. However, the research focus of this paper is confined to the tail car. In fact, the aerodynamic shape of the entire train will influence the wake field. Future research should incorporate more studies for diverse running speeds, tunnel cross-sectional areas, bogie

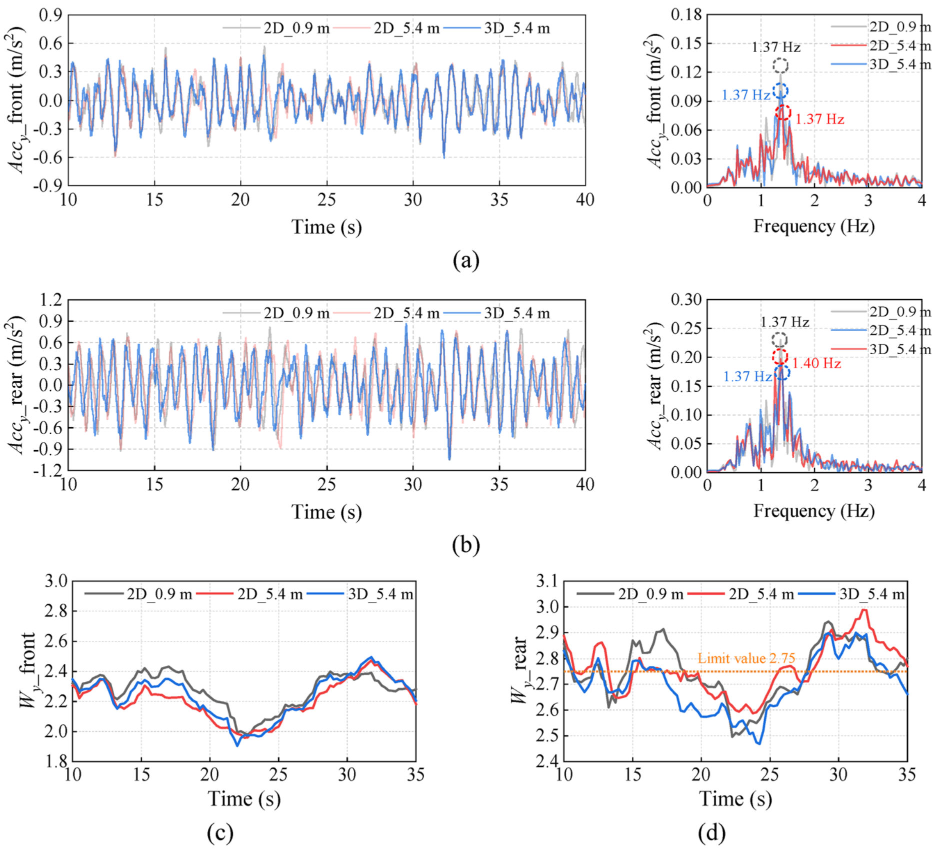

FIG. 21. Time and frequency domain of Acc_y and W_y under 2D and 3D head shapes: (a) Acc_y at front end. (b) Acc_y at rear end. (c) W_y at front end. (d) W_y at rear end.

TABLE X. Statistics of W_y under 2D and 3D head shapes.

Position	Head shape	Maximum	Minimum	Average
Front end	2D_0.9 m	2.43	1.98	2.27
	2D_5.4 m	2.47	1.96	2.21
	3D_5.4 m	2.50	1.91	2.24
Rear end	2D_0.9 m	2.94	2.50	2.75
	2D_5.4 m	2.99	2.59	2.76
	3D_5.4 m	2.90	2.47	2.70

cladding, the windshield between carriages, and the height of the carbody bottom from the ground. These will facilitate a comprehensive understanding of the influence of the train's aerodynamic shape on aerodynamic loads and vehicle dynamic responses.

ACKNOWLEDGMENTS

This work was supported by the National Natural Science Foundation of China (Grant Nos. 52372403 and U2268211), the National Railway Group Science and Technology Program (Grant No. N2023J071), and the Southwest Jiaotong University-Lanzhou Jiaotong University Joint Innovation Fund Project (Grant No. 2682023ZTZ001).

AUTHOR DECLARATIONS

Conflict of Interest

The authors have no conflicts to disclose.

Author Contributions

Ting Qin: Conceptualization (equal); Data curation (equal); Formal analysis (equal); Methodology (equal); Writing – original draft (equal). **Yuan Yao**: Conceptualization (equal); Funding acquisition (equal); Project administration (equal); Resources (equal); Writing – review & editing (equal). **Yadong Song**: Investigation (equal); Validation (equal); Writing – review & editing (equal).

DATA AVAILABILITY

The data that support the findings of this study are available from the corresponding author upon reasonable request.

REFERENCES

[1]W. Li, Q. H. Guan, M. R. Chi, Z. F. Wen, and J. F. Sun, "An investigation into the influence of wheel-rail contact relationships on the carbody hunting stability of an electric locomotive," Proc. Inst. Mech. Eng., Part F **236**(10), 1198–1209 (2022).
[2]J. F. Sun, M. R. Chi, X. S. Jin, S. L. Liang, J. Wang, and W. Li, "Experimental and numerical study on carbody hunting of electric locomotive induced by low wheel-rail contact conicity," Veh. Syst. Dyn. **59**(2), 203–223 (2021).

[3]Y. X. Shi, H. Y. Dai, Q. S. Wang, L. Wei, and H. L. Shi, "Research on low-frequency swaying mechanism of metro vehicles based on wheel-rail relationship," Shock Vib. **2020**(12), 1–15.
[4]G. Li, Y. Yao, L. J. Shen, X. X. Deng, and W. S. Zhong, "The influence of yaw damper layouts on locomotive lateral dynamics performance: Pareto optimization and parameter analysis," J. Zhejiang Univ. Sci. A **24**(5), 450–464 (2023).
[5]Y. Yao, Z. F. Xu, Y. D. Song, L. J. Shen, and C. L. Li, "Mechanism of train tail lateral sway of EMUs in tunnel based on vortex-induced vibration," J. Traffic Transp. Eng. **21**(5), 114–124 (2021) (in Chinese).
[6]H. Fujimoto, M. Miyamoto, and Y. Shimamoto, "Lateral vibration and its decreasing measure in the tail car of a Shinkansen," Trans. Jpn. Soc. Mech. Eng. **59**(560), 1016–1022 (1993).
[7]H. Takai, "Maintenance of track with long-wave track irregularity on Shinkansen," Railw. Tech. Res. Inst., Q. Rep. **31**(3), 128–131 (1990).
[8]M. Suzuki, "Unsteady aerodynamic force acting on high speed trains in tunnel," Q. Rep. RTRI **42**(2), 89–93 (2001).
[9]M. Suzuki, "An experimental study on aerodynamic force acting on train in tunnel," in *Proceedings of International Symposium on Seed-up and Service Technology for Railway and Maglev Systems 2003: STECH'03* (Japan Society of Mechanical Engineers, 2003), pp. 395–397.
[10]M. Suzuki, "Flow-induced vibration of high-speed trains in tunnels," in *The Aerodynamics of Heavy Vehicles: Trucks, Buses, and Trains* (Springer, Berlin, Heidelberg, 2004), Vol. 19, pp. 443–452.
[11]B. Diedrichs, M. Berg, S. Stichel, and S. Krajnović, "Vehicle dynamics of a high-speed passenger car due to aerodynamics inside tunnels," Proc. Inst. Mech. Eng., Part F **221**(4), 527–545 (2007).
[12]B. Diedrichs, S. Kajović, and M. Berg, "On the aerodynamics of car body vibrations of high-speed trains cruising inside tunnels," Eng. Appl. Comput. Fluid Mech. **2**(1), 51–57 (2008).
[13]K. Tanifuji, K. Sakanoue, and S. Kikko, "Modelling of aerodynamic force acting on high speed train in tunnel and a measure to improve the riding comfort utilising restriction between cars," Veh. Syst. Dyn. **46**(sup1), 1065–1075 (2008).
[14]J. K. Choi and K. H. Kim, "Effects of nose shape and tunnel cross-sectional area on aerodynamic drag of train traveling in tunnels," Tunnelling Underground Space Technol. **41**, 62–73 (2014).
[15]S. B. Wang, D. Burton, A. Herbst, J. Sheridan, and M. Thompson, "The effect of bogies on high-speed train slipstream and wake," J. Fluids Struct. **83**, 471–489 (2018).
[16]Z. W. Zhou, C. Xia, X. Z. Shan, and Z. G. Yang, "The impact of bogie sections on the wake dynamics of a high-speed train," Flow. Turbul. Combust. **104**(1), 89–113 (2020).
[17]J. R. Bell, D. Burton, M. C. Thompson, A. H. Herbst, and J. Sheridan, "The effect of tail geometry on the slipstream and unsteady wake structure of high-speed trains," Exp. Therm. Fluid Sci. **83**, 215–230 (2017).
[18]H. Hemida and S. Krajnović, "Exploring flow structures around a simplified ICE2 train subjected to a 30 degrees side wind using LES," Eng. Appl. Comput. Fluid Mech. **3**(1), 28–41 (2009).
[19]H. Hemida and S. Krajnović, "LES study of the influence of the nose shape and yaw angles on flow structures around trains," J. Wind Eng. Ind. Aerodyn. **98**(1), 34–46 (2010).
[20]A. Khayrullina, B. Blocken, W. Janssen, and J. Straathof, "CFD simulation of train aerodynamics: Train-induced wind conditions at an underground railroad passenger platform," J. Wind Eng. Ind. Aerodyn. **139**(24), 100–110 (2015).
[21]T. Li, M. G. Yu, J. Y. Zhang, and W. H. Zhang, "A fast equilibrium state approach to determine interaction between stochastic crosswinds and high-speed trains," J. Wind Eng. Ind. Aerodyn. **143**, 91–104 (2015).
[22]T. Li, J. Y. Zhang, and W. H. Zhang, "An improved algorithm for fluid-structure interaction of high-speed trains under crosswind," J. Mod. Transp. **19**(2), 75–81 (2011).
[23]T. Cui, W. H. Zhang, and B. C. Sun, "Research method and application of fluid-structure coupling vibration for high-speed train," J. China Railw. Soc. **35**(4), 16–22 (2013) (in Chinese).
[24]Z. L. Ji, W. Liu, D. L. Guo, G. W. Yang, and J. Mao, "Analysis of the fluid–structure coupling characteristics of a high-speed train passing through a tunnel," Int. J. Struct. Stab. Dyn. **22**(16), 2250185 (2022).
[25]G. J. Li and X. B. Zhong, "Research on lateral sway and suspension optimization of tail vehicle in a city EMU," Electr. Locomot. Mass Transit Veh. **45**(6), 26–31 (2022).
[26]P. Han, E. de Langre, M. C. Thompson, K. Hourigan, and J. S. Zhao, "Vortex-induced vibration forever even with high structural damping," J. Fluid Mech. **962**, A13 (2023).
[27]C. H. K. Williamson and R. Govardhan, "Vortex-induced vibration," Annu. Rev. Fluid Mech. **36**(1), 413–455 (2004).
[28]H. Y. Yu, O. Øiseth, M. J. Zhang, F. Y. Xu, and G. Hu, "Tuned mass damper design for vortex-induced vibration control of a bridge: Influence of vortex-induced force model," J. Bridge Eng. **28**(5), 04023021 (2023).
[29]G. Q. Zhang, Y. L. Xu, B. Wang, and Q. Zhu, "Turbulence effects on vortex-induced dynamic response of a twin-box bridge and ride comfort of the vehicle," Int. J. Struct. Stab. Dyn. **23**(16n18), 2340023 (2023).
[30]X. Zhao, M. Tan, W. D. Zhu, T. B. Shao, and Y. H. Li, "Study of vortex-induced vibration of a pipe-in-pipe system by using a wake oscillator model," J. Environ. Eng. **149**(4), 04023007 (2023).
[31]D. J. Liu, X. Z. Li, F. L. Mei, L. F. Xin, and Z. G. Zhou, "Effect of vertical vortex-induced vibration of bridge on railway vehicle's running performance," Veh. Syst. Dyn. **61**(5), 1432–1447 (2023).
[32]Y. D. Song, T. Qin, Y. Yao, and F. Y. Dai, "Investigation on aerodynamic fluid-structure coupling vibration of 160 km/h EMU tail in single-track tunnels," Int. J. Struct. Stab. Dyn. **24**(18), 2450197 (2024).
[33]Y. D. Song, Y. Yao, M. Lu, and X. Wang, "Mechanism and improvement for tail vehicle swaying of powercentralized EMUs," Proc. Inst. Mech. Eng., Part F **238**(10), 1296–1306 (2024).
[34]Y. D. Song, Y. P. Zou, Y. Yao, and L. J. Shen, "Aerodynamics and countermeasures of train tail swaying inside single-track tunnels," J. Zhejiang Univ.-SCI. A **26**, 438–455 (2024).
[35]CEN, "Railway applications aerodynamics Part 6: Requirements and test procedures for cross wind assessment," Report No. EN 14064-6 (CEN, 2018).
[36]Ministry of Railways of the People's Republic of China, "Standard gauge railway rolling stock clearance and structure clearance classification and basic dimensions," Report No. GB 146-2 (Ministry of Railways of the People's Republic of China, 2020).
[37]National Railway Administration, "Code for design of high-speed railway," Report No. TB 10621-2014 (National Railway Administration, 2014).
[38]National Railway Administration, "Code for design of railway tunnels," Report No. TB 10003-2016 (National Railway Administration, 2016).
[39]National Railway Administration of People's Republic of China, "Specification for dynamics performance assessment and testing verification of rolling stock," Report No. GB T5599 (National Railway Administration of People's Republic of China, 2019).
[40]W. Liu, D. L. Guo, Z. J. Zhang, D. W. Chen, and G. W. Yang, "Effects of bogies on the wake flow of a high-speed train," Appl. Sci. **9**(4), 759 (2019).